



Using the Impulse–Response Pile Data for Soil Characterization

Heeyong Huh¹; Heedong Goh²; Jun Won Kang³; Stijn François⁴; and Loukas F. Kallivokas, M.ASCE⁵

Abstract: The impulse–response (IR) test is the most commonly used field procedure for assessing the structural integrity of piles embedded in soil. The IR test uses the response of the pile to waves induced by an impulse load applied at the pile head in order to assess the condition of the pile. However, due to the contact between the pile and the soil, the recorded response at the pile head carries information not only about the pile, but about the soil as well, thus creating the as-yet-unexplored opportunity to characterize the properties of the surrounding soil. In effect, such dual use of the IR test data renders piles into probes for characterizing the near-surface soil deposits and/or soil erosion along the pile–soil interface. In this article, we discuss a systematic full-waveform-based inversion methodology that allows imaging of the soil surrounding a pile using conventional IR test data. We adopt a heterogeneous Winkler model to account for the effect of the soil on the pile’s response, and the pile’s end is assumed to be elastically supported, thus also accounting for the underlying soil. We appeal to a partial differential equation (PDE)-constrained-optimization approach, where we seek to minimize the misfit between the recorded time-domain response at the pile head (the IR data), and the response due to trial distributions of the spatially varying soil stiffness, subject to the coupled pile–soil wave propagation physics. We report numerical experiments involving layered soil profiles for piles founded on either soft or stiff soil, where the inversion methodology successfully characterizes the soil. DOI: [10.1061/JENMDT.EMENG-6865](https://doi.org/10.1061/JENMDT.EMENG-6865). © 2023 American Society of Civil Engineers.

Introduction

The analysis of dynamic soil–structure interaction problems and the evaluation of seismic site effects requires characterization of the dynamic properties of the shallow soil layers. Typical needs arise in the aseismic design of infrastructure components (Kausel 2010), or in the analysis of vibration effects in the built environment (Lombaert et al. 2015). The dynamic soil properties, which typically include the low-strain shear and dilational wave velocities, can be determined by either laboratory tests or in situ methods. Laboratory tests, such as bender element tests and resonant column tests, are well-established, but sample preparation may influence the measurements (Rix et al. 2000).

Alternatively, the in situ evaluation of dynamic soil properties include borehole and surface methods. Borehole methods (e.g., cross-hole and downhole tests) (Stokoe et al. 1978; Bregman et al. 1989) provide a good resolution of the dynamic soil properties with depth,

but are invasive, laborious, and expensive because boreholes are required. Surface methods, such as the spectral analysis of surface waves (SASW) method (Nazarian and Desai 1993; Stokoe et al. 1994), and its successor, the multichannel analysis of surface waves (MASW) (Park et al. 1999), are based on measurements of free-field vibrations generated by impacting the soil’s surface. Surface methods are nonintrusive and relatively easy to perform, but have limited resolution at larger depths (Schevenels et al. 2008), are plagued by near-field effects, and are inherently one-dimensional methods. More generally, the identification of soil properties from in situ measurements relies on the solution of an inverse medium problem. Commonly, the assumption of a horizontally layered medium is made to make this inversion more tractable, but, recently, full-waveform inversion techniques have emerged that do not rest on such assumptions (Kallivokas et al. 2013; Fathi et al. 2015, 2016) and are viewed as the most promising for reconstructing the soil profiles at shallow depths.

In assessing seismic risk to existing pile foundations or when evaluating remaining service life, the condition assessment of piles is also of importance. It is most often the case that the condition assessment of piles embedded in soil is carried out without taking into account the coupling effects with the surrounding soil [for example, the nondestructive methods described by Rausche et al. (1985) and Holeyman (1992)]. Methods are based on either high-strain and low-strain dynamic pile loading. High-strain dynamic pile testing involves high impact loading, where the force applied at the pile head and the pile head velocity are monitored during the impact. The main objective of high-strain dynamic pile testing is to verify the ultimate bearing capacity of the pile, and the load amplitude should be sufficiently high to mobilize the pile capacity (Hertlein and Davis 2007). High-strain dynamic pile testing involves signal matching of the measured signal with a numerical model of wave propagation along the pile, and various signal matching procedures of varying complexity have been proposed (Middendorp and Verbeek 2004), such as CAPWAP

¹Dept. of Aerospace Engineering and Engineering Mechanics, Univ. of Texas at Austin, Austin, TX 78712. ORCID: <https://orcid.org/0000-0003-0257-2718>. Email: heeyonghuh@utexas.edu

²Dept. of Civil, Architectural, and Environmental Engineering, Univ. of Texas at Austin, Austin, TX 78712. ORCID: <https://orcid.org/0000-0003-4854-6435>. Email: heedong.goh@utexas.edu

³Dept. of Civil Engineering, Hongik Univ., Wausan-ro 94, Mapo-gu, Seoul 04066, Korea. Email: jwkang@hongik.ac.kr

⁴Dept. of Civil Engineering, Katholieke Universiteit (KU) Leuven, Leuven, Belgium. ORCID: <https://orcid.org/0000-0002-3877-9748>. Email: stijn.francois@bwk.kuleuven.be

⁵Dept. of Civil, Architectural, and Environmental Engineering, Univ. of Texas at Austin, Austin, TX 78712 (corresponding author). ORCID: <https://orcid.org/0000-0002-7701-6989>. Email: loukas@mail.utexas.edu

Note. This manuscript was submitted on July 13, 2022; approved on May 23, 2023; published online on July 31, 2023. Discussion period open until December 31, 2023; separate discussions must be submitted for individual papers. This paper is part of the *Journal of Engineering Mechanics*, © ASCE, ISSN 0733-9399.

(Rausche et al. 2000), TNOWAVE (Courage and Bielefeld 1992), and GRLWEAP (Rausche et al. 1992).

In contrast, low-strain dynamic pile test methods aim at verifying pile integrity, where in practical applications the impact sources are instrumented hammers, or low-amplitude harmonic vibration shakers. A distinction should be made between the sonic-echo test and the impulse-response test: the sonic-echo test is performed by measuring the pile head velocity due to (low-amplitude) hammer impact, whereas in the impulse-response (IR) test, the hammer force is also measured using an instrumented hammer. The IR test is the most frequently used test for assessing piles (Baxter et al. 2004; Davis 2003; Finno and Gassman 1998; Liao and Roësset 1997; Rausche 2004), and is considered cost-effective due to the ease of the associated field procedures. The IR test is used to assess the material properties of the pile, or its geometric properties (cross-sectional area and length), and more rarely both; exceptions, using a signal-matching inversion procedure, include the studies by Shahram and Fakharian (2008) and Warrington (2016).

The two interests—soil characterization and pile condition assessment—have been, by and large, treated separately: whereas characterizing the soil prior to construction remains of critical importance, postconstruction condition assessment of the coupled soil-pile system should not treat each medium separately because the coupled effects cannot be ignored (Ekanayake et al. 2013; Phuong et al. 2016). Although the literature is very rich in reports of both field and numerical investigations of dynamic soil-pile interactions (e.g., Seylabi et al. 2017), due to its complexity, the associated inverse problem has not been treated in a systematic manner.

In earnest, a complete imaging of both the soil and the pile would require that one inverts for the spatially distributed properties of both media; this includes Young's modulus, mass density, cross-sectional area, and length of the pile, in addition to soil parameters. From an inversion perspective, the task is daunting, and, to date, has not been attempted. It is only recently that a semiempirical process has been reported (Yu et al. 2022), where the IR data have been used to simultaneously assess the pile's and the soil's characteristics, but a bona fide inversion process has yet to be reported.

In this paper, we address the as-yet-unexplored use of IR measurements to characterize the soil properties in the vicinity of the pile. The key idea explored in this paper is that the recorded response at the pile head carries information not only about the pile, but about the soil as well due to the dynamic interaction between the pile and the soil. Therefore, the IR test may allow to also characterize the properties of the surrounding soil. In effect, such dual use of the IR test data treats the pile as a probe, tasked with inferring

the dynamic soil properties in the vicinity of the pile, and the method could possibly also be used to detect erosion or pile-soil gaps (Radhima et al. 2021) along the pile shaft. The explanation of the methodology makes three key assumptions: (1) the soil in the vicinity of the pile, although arbitrarily heterogeneous in depth, is horizontally layered, (2) the soil is in contact with the pile along the pile's entire length, and (3) the induced soil response remains in the small-strain regime. The first assumption does not preclude lateral heterogeneity away from the pile's immediate vicinity (e.g., within a pile radius away from the pile), and the second assumption still allows for weak pile-soil bonding to be captured in the form of reduced soil stiffness.

This paper is organized as follows: in the next section, the dynamic soil-pile model is introduced, where a heterogeneous Winkler model is used to represent the soil surrounding an uncapped axially loaded pile. The two most salient issues of the forward problem are discussed, namely, the dispersive characteristics of the coupled soil-pile problem and the sensitivity of the pile head response to variations of the soil properties. In the following section, the soil-pile model is used to formulate the IR-based soil characterization as a partial differential equation (PDE)-constrained optimization problem. A full-waveform inversion technique is proposed, where the misfit between the recorded time-domain response at the pile head (the IR data) is minimized. The numerical implementation of the proposed methodology is discussed next, followed by the Numerical Examples section, where we present the results from four numerical experiments based on the proposed methodology. The main conclusions are summarized in the last section.

Pile Embedded in Soil: Preliminary Considerations

The Forward Problem

Consider a homogeneous pile embedded in soil [Fig. 1(a)]. The pile has length L , constant Young's modulus E , mass density ρ , and cross-sectional area A . The surrounding soil is assumed to be heterogeneous and is modeled using the Winkler hypothesis: its distributed stiffness per unit length is denoted with $k(x)$, where x is the axial coordinate measured from the pile head. The pile rests on a soil layer, whose stiffness, following again a Winkler hypothesis, is denoted with k_b ; the pile head is subjected to a dynamic load $P(t)$ [Fig. 1(b)]. The Winkler model is the simplest one can use to represent the soil and is adopted herein precisely because of its simplicity and common use in practice (Chin and Poulos 1991; Crispin et al. 2018); however, the described methodology can readily

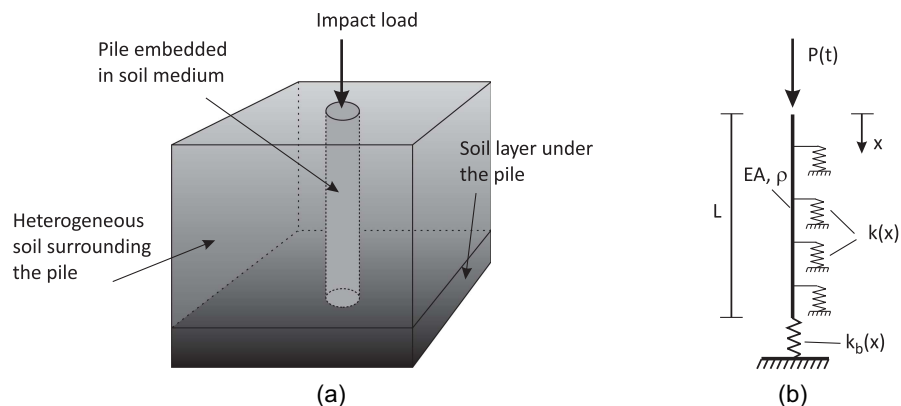


Fig. 1. Pile embedded in soil: (a) physical model; and (b) mathematical idealization.

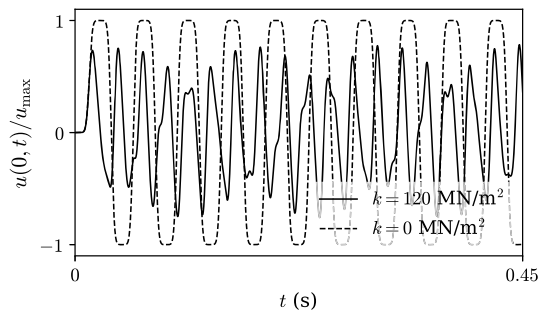


Fig. 2. Typical response of a pile fixed at its end ($k_b = \infty$) when subjected to a Gaussian pulse head load: (a) no surrounding soil (dashed line) and $k(x) = 0$; and (b) pile embedded in soil (solid line) and $k(x) = k_0 = 120 \text{ MN/m}^2$.

accommodate more sophisticated soil models (e.g., Takemiya and Yamada 1981; Holeyman and Whenham 2015) without substantial changes to the approach.

The wave-propagation physics associated with the mathematical model shown in Fig. 1(b) can be described by the following PDE:

$$\frac{\partial}{\partial x} \left(EA \frac{\partial u}{\partial x} \right) - ku - \rho A \frac{\partial^2 u}{\partial t^2} = 0, \quad x \in (0, L), t \in (0, T) \quad (1)$$

subject to the following boundary conditions:

$$EA \frac{\partial u}{\partial x} + P = 0, \quad x = 0, t \in (0, T) \quad (2a)$$

$$EA \frac{\partial u}{\partial x} + k_b u = 0, \quad x = L, t \in (0, T) \quad (2b)$$

and initial conditions of

$$u = 0, \quad t = 0, x \in (0, L) \quad (3a)$$

$$\frac{\partial u}{\partial t} = 0, \quad t = 0, x \in (0, L) \quad (3b)$$

where $u \equiv u(x, t)$ = axial pile displacement.

Consider next a typical application of an IR test: the pile head ($x = 0$) is subjected to a Gaussian pulse, and the response $u(0, t)$ is recorded at the same point. Fig. 2 depicts the normalized response at the pile head for two contrasting cases: (1) when the effect of the surrounding soil is ignored [$k(x) = 0$]; and (2) when the soil is taken into account [$k(x) = k_0 \neq 0$]. In both cases, it is assumed that the pile rests on bedrock ($k_b = \infty$).

As it can be seen, the two traces differ significantly: the difference is due to the soil, and it is precisely this difference in the record that we seek to exploit to infer the properties of the soil. Said differently, the head record contains information about the surrounding soil properties (and, in general, of the underlying soil too when $k_b \neq \infty$), which we seek to reveal by, effectively, using the piles as probes.

Dispersion and the Cutoff Frequency

In a free-standing pile [no surrounding soil and $k(x) = 0$], waves propagate at a single velocity $c = \sqrt{E/\rho}$. However, the presence of the soil leads to dispersive behavior, where waves propagate at different frequency-dependent speeds. The behavior is typically captured by the dispersion relation, which connects the spatial wave number ξ to the frequency f . For constant soil stiffness $k(x) = k_0$ and for an infinitely long pile fixed at its end, the dispersion relation reads

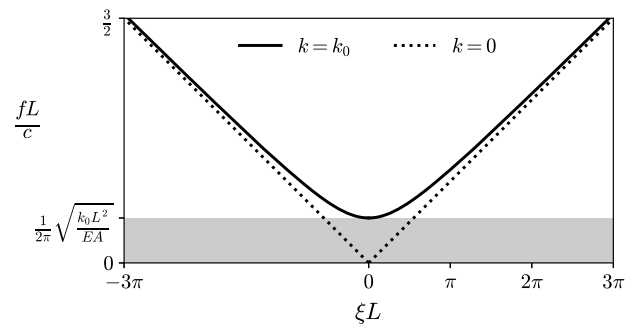


Fig. 3. Dispersion curve of a pile with $k(x) = k_0$ (solid line) and $k(x) = 0$ (dotted line). The shaded region below the cutoff frequency depicts a band gap.

$$\xi^2 = \left(\frac{2\pi f}{c} \right)^2 - \frac{k_0}{EA} \quad (4)$$

Fig. 3 depicts the dispersion behavior for two cases, corresponding to $k(x) = k_0$ (solid line = dispersive) and $k(x) = 0$ (dotted line = nondispersive), respectively.

Of importance is the shaded region between the origin and the cutoff frequency f_c , which can be obtained by enforcing the vanishing of the right-hand-side of the dispersion relation Eq. (4)

$$f_c = \frac{1}{2\pi} \sqrt{\frac{k_0}{\rho A}} \quad \text{or} \quad \frac{f_c L}{c} = \frac{1}{2\pi} \sqrt{\frac{k_0 L^2}{EA}} \quad (5)$$

Below the cutoff frequency, waves do not propagate and, consequently, to be able to use the pile as a probe, it is imperative that the frequency spectrum of the head load lies above the cutoff frequency f_c . In general, when the soil stiffness $k(x)$ varies along the pile length, the dispersion relation is more complicated than Eq. (4): there can be multiple band gaps such as the shaded region of Fig. 3, as indeed is the case with layered soils.

However, it can be shown, that the stiffness of the underlying soil k_b does not impact the (first) cutoff frequency: consider, for example, a pile with $L = 45 \text{ m}$, $\rho = 2,400 \text{ kg/m}^3$, $E = 40 \text{ MN/m}^2$, $A = 1 \text{ m}^2$, and $k_0 = 120 \text{ MN/m}^2$. Then, using Eq. (5), the cutoff frequency is $f_c \approx 35 \text{ Hz}$. To illustrate the effect of the cutoff frequency and its invariance with respect to k_b , the pile head is subjected to two different Gaussian pulses, whose spectral bandwidth is $f_b = 20 \text{ Hz}$, and $f_b = 200 \text{ Hz}$, respectively (the Appendix gives a definition of the spectral bandwidth). In the first case, the pulse's frequency content lies below the cutoff frequency ($f_b < f_c$), i.e., it is fully contained in the band gap, whereas in the second case, a good portion of the pulse's frequency content is within the pass-band of the dispersion plot.

Fig. 4 depicts the time histories of the displacement computed at the pile head for the two Gaussian pulses, and for two different values of k_b . In Fig. 4(a), the Gaussian pulse with the subcutoff frequency content does not promote the propagation of waves for either of the two k_b values, whereas in Fig. 4(b), in the case of the Gaussian pulse with the wider f_b spectrum, waves propagate and in fact result in different traces for the two different k_b values.

In conclusion, provided that the frequency content of the pile head excitation is within the pass-bands of the dispersion relation, even if partially, then the time trace of the response at the pile head is sufficiently sensitive to variations of the soil properties to allow for their determination via full-waveform inversion, as outlined in the next section.

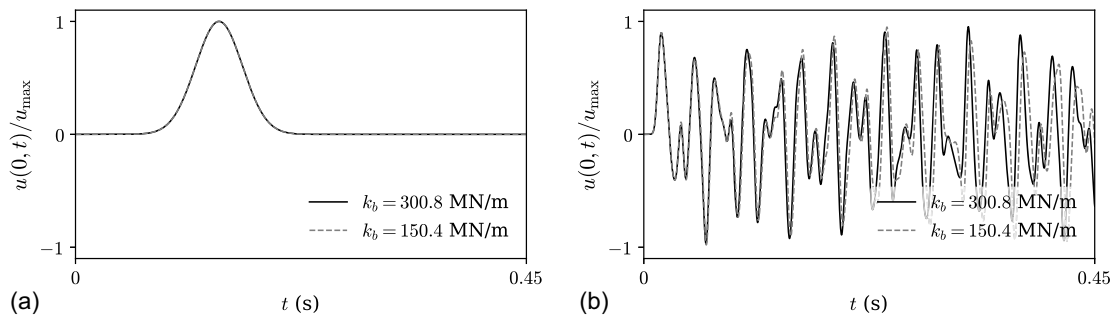


Fig. 4. Pile head displacement histories for two Gaussian pulses with $f_b = 20$ Hz and $f_b = 200$ Hz: (a) response due a Gaussian pulse with spectrum in the band gap ($f_b = 20$ Hz), where there is no propagation for any k_b ; and (b) response due a Gaussian pulse with spectrum in the pass-band ($f_b = 200$ Hz), where waves propagate and the response is sensitive to k_b .

Using the IR Data for Soil Characterization

In this section, we follow established lines of PDE-constrained optimization (Biegler et al. 2003; De Los Reyes 2015; Fathi et al. 2015) to invert for the properties of the soil in contact with the embedded pile [$k(x)$ and k_b] when given time-domain records of the applied load at the pile head and of the resulting motion recorded also at the pile head; throughout, we also assume that the pile properties (EA and L) are known a priori. In general, $k(x)$ is assumed to vary arbitrarily with respect to x , i.e., there is no need to assume that the surrounding soil is, for example, layered. Consequently, the number of unknown material parameters that need to be determined in order to recover the soil profile depends on the numerical discretization scheme one uses to resolve the propagation of waves, and, in general, is in the hundreds or thousands: the inverse problem of determining the soil properties based on a single time-domain record is ill-posed and prone to solution multiplicity.

Full-Waveform Inverse Problem

Our starting point is the introduction of a Lagrangian functional \mathcal{L} , comprising a misfit functional \mathcal{F}_m , a regularization term $\mathcal{R}(k)$ associated with the soil properties $k(x)$, and the side imposition via adjoint variables (or Lagrange multipliers) of the forward initial- and boundary-value problem defined in Eqs. (1)–(3). Accordingly, let

$$\begin{aligned} \mathcal{L}(u, \lambda, \lambda_0, \lambda_L, k, k_b) &= \mathcal{F}_m + \mathcal{R}(k) + \int_0^L \int_0^T \lambda \left[\frac{\partial}{\partial x} \left(EA \frac{\partial u}{\partial x} \right) - ku - \rho A \frac{\partial^2 u}{\partial t^2} \right] dt dx \\ &+ \int_0^T \lambda_0 \left[EA \frac{\partial u}{\partial x} + P(t) \right] \Big|_{x=0} dt \\ &+ \int_0^T \lambda_L \left[EA \frac{\partial u}{\partial x} + k_b u \right] \Big|_{x=L} dt \end{aligned} \quad (6)$$

where T = total period of observations; $\lambda(x, t)$, $\lambda_0(t)$, and $\lambda_L(t)$ = adjoint variables; and misfit functional \mathcal{F}_m = difference, in the least-squares sense, between the calculated $u(0, t)$ and the measured or recorded pile head displacements $u_m(0, t)$, normalized by the square of the measured response, i.e., as follows:

$$\mathcal{F}_m := \frac{1}{2} \frac{\int_0^T [u(0, t) - u_m(0, t)]^2 dt}{\int_0^T [u_m(0, t)]^2 dt} \quad (7)$$

As is often the case with inverse problems, here too there can be multiple solutions for $k(x)$ and k_b that would simultaneously minimize the misfit \mathcal{F}_m and satisfy the forward problem: the inclusion of the regularization term $\mathcal{R}(k)$ in Eq. (6) of the Lagrangian \mathcal{L}

aims at the alleviation of the solution multiplicity. In this work, we explore two regularization schemes: a first-order Tikhonov (TN), and a total-variation (TV) regularization scheme. The corresponding regularization functionals $\mathcal{R}(k)$ for each of the two regularization schemes are defined as

$$\begin{aligned} \mathcal{R}^{\text{TN}}(k) &:= \frac{1}{2} R \int_0^L \left(\frac{dk}{dx} \right)^2 dx, \\ \mathcal{R}^{\text{TV}}(k) &:= R \int_0^L \left[\left(\frac{dk}{dx} \right)^2 + \epsilon \right]^{\frac{1}{2}} dx \end{aligned} \quad (8)$$

where ϵ = small number. The regularization factor R controls the amount by which the Lagrangian is penalized by the regularization term, relative to the misfit. In general, the TN scheme penalizes the high-frequency spatial oscillations of the soil properties $k(x)$, thereby eliminating any spatially rapid nonphysical property transitions, thereby enforcing smooth profiles. In contrast, the TV scheme, which is defined as the bounded variation seminorm of $k(x)$, tends to preserve discontinuities of $k(x)$, such as those that may arise in layered soil profiles, while also penalizing spurious property oscillations in smooth regions. To find the properties $k(x)$ and k_b that minimize the Lagrangian is equivalent to finding the properties that simultaneously minimize the misfit and satisfy the underlying PDE that describes the propagating waves.

Optimality Conditions

Next, we search for a stationary point of the Lagrangian by seeking to satisfy the first-order optimality conditions. Accordingly, we require that the first variation $\delta_u \mathcal{L}$ of \mathcal{L} with respect to the state variable $u(x, t)$, the first variations $\delta_\lambda \mathcal{L}$, $\delta_{\lambda_0} \mathcal{L}$, and $\delta_{\lambda_L} \mathcal{L}$ of \mathcal{L} with respect to the adjoint variables $\lambda(x, t)$, $\lambda_0(t)$, and $\lambda_L(t)$, and the first variations $\delta_k \mathcal{L}$ and $\delta_{k_b} \mathcal{L}$ of \mathcal{L} with respect to the sought-after properties $k(x)$ and k_b (or control parameters), all vanish. Specifically, enforcing the vanishing of the first variation of \mathcal{L} with respect to λ , λ_0 , and λ_L results in

$$\delta_\lambda \mathcal{L} = 0 \Rightarrow \int_0^L \int_0^T \delta \lambda \left[\frac{\partial}{\partial x} \left(EA \frac{\partial u}{\partial x} \right) - ku - \rho A \frac{\partial^2 u}{\partial t^2} \right] dt dx = 0 \quad (9)$$

$$\delta_{\lambda_0} \mathcal{L} = 0 \Rightarrow \int_0^T \delta \lambda_0 \left[EA \frac{\partial u}{\partial x} + P(t) \right] \Big|_{x=0} dt = 0 \quad (10)$$

$$\delta_{\lambda_L} \mathcal{L} = 0 \Rightarrow \int_0^T \delta \lambda_L \left[EA \frac{\partial u}{\partial x} + k_b u \right] \Big|_{x=L} dt = 0 \quad (11)$$

Because $\delta\lambda$, $\delta\lambda_0$, and $\delta\lambda_L$ are arbitrary, it can be readily deduced that Eqs. (9)–(11) recover the forward problem defined previously in Eqs. (1)–(3).

Enforcing the vanishing of the first variation of \mathcal{L} with respect to $u(x, t)$ yields

$$\begin{aligned} \delta_u \mathcal{L} &= 0 \\ \Rightarrow \int_0^T [u(0, t) - u_m(0, t)] \delta u(0, t) dt \\ &+ \int_0^L \int_0^T \lambda \left[\frac{\partial}{\partial x} \left(EA \frac{\partial \delta u}{\partial x} \right) - k \delta u - \rho A \frac{\partial^2 \delta u}{\partial t^2} \right] dt dx \\ &+ \int_0^T \lambda_0 EA \frac{\partial \delta u}{\partial x} \Big|_{x=0} dt + \int_0^T \lambda_L \left[EA \frac{\partial \delta u}{\partial x} + k_b \delta u \right] \Big|_{x=L} dt = 0 \end{aligned} \quad (12)$$

Using integration by parts while also taking into account the initial conditions [Eq. (3)] and after rearranging terms, Eq. (12) can be rewritten

$$\begin{aligned} \int_0^T \delta u(0, t) \left[EA \frac{\partial \lambda}{\partial x}(0, t) + [u(0, t) - u_m(0, t)] \right] dt \\ + \int_0^L \int_0^T \delta u(x, t) \left[\frac{\partial}{\partial x} \left(EA \frac{\partial \lambda}{\partial x} \right) - k \lambda - \rho A \frac{\partial^2 \lambda}{\partial t^2} \right] dt dx \\ + \int_0^T \frac{\partial \delta u}{\partial x}(L, t) [EA \lambda(L, t) + EA \lambda_L(t)] dt \\ + \int_0^T \delta u(L, t) \left[-EA \frac{\partial \lambda}{\partial x}(L, t) + k_b \lambda_L(t) \right] dt \\ + \int_0^T \frac{\partial \delta u}{\partial x}(0, t) [EA \lambda_0(t) - EA \lambda(0, t)] dt \\ - \int_0^L \rho A \frac{\partial \delta u}{\partial t}(x, T) \lambda(x, T) dx + \int_0^L \rho A \delta u(x, T) \frac{\partial \lambda}{\partial t}(x, T) dx = 0 \end{aligned} \quad (13)$$

Considering the arbitrariness of the variations implicated in the preceding, Eq. (13) results in the adjoint problem for $\lambda(x, t)$, which is defined as follows:

$$\frac{\partial}{\partial x} \left(EA \frac{\partial \lambda}{\partial x} \right) - k \lambda - \rho A \frac{\partial^2 \lambda}{\partial t^2} = 0, \quad x \in (0, L), t \in (0, T) \quad (14)$$

subject to the following boundary conditions:

$$EA \frac{\partial \lambda}{\partial x} = -(u - u_m), \quad x = 0, t \in (0, T) \quad (15a)$$

$$EA \frac{\partial \lambda}{\partial x} + k_b \lambda = 0, \quad x = L, t \in (0, T) \quad (15b)$$

and final-value conditions

$$\lambda = 0, \quad x \in (0, L), t = T \quad (16a)$$

$$\frac{\partial \lambda}{\partial t} = 0, \quad x \in (0, L), t = T \quad (16b)$$

From Eq. (13), it also holds that

$$\lambda_L(t) = -\lambda(L, t), \quad \text{and} \quad \lambda_0(t) = \lambda(0, t) \quad (17)$$

Having obtained the forward and the adjoint problems, there remains to seek to satisfy the third optimality condition by requiring the vanishing of the first variations of \mathcal{L} with respect to $k(x)$ and k_b , respectively. Accordingly

$$\delta_k \mathcal{L} = 0$$

$$\begin{aligned} \Rightarrow R \int_0^L \frac{dk}{dx} \frac{d\delta k}{dx} dx - \int_0^L \int_0^T \lambda u \delta k dt dx = 0 \\ \Rightarrow R \left[\frac{dk}{dx} \delta k \right]_0^L - R \int_0^L \delta k \frac{d^2 k}{dx^2} dx - \int_0^L \int_0^T \delta k \lambda u dt dx = 0 \\ \Rightarrow R \frac{dk}{dx}(L) \delta k(L) - R \frac{dk}{dx}(0) \delta k(0) \\ + \int_0^L \delta k \left[-R \frac{d^2 k}{dx^2} - \int_0^T \lambda u dt \right] dx = 0 \end{aligned} \quad (18)$$

Because $\delta k(x)$, $\delta k(L)$, and $\delta k(0)$ are arbitrary, there results the following boundary-value problem for $k(x)$:

$$g^k(x) = -R \frac{d^2 k(x)}{dx^2} - \int_0^T \lambda(x, t) u(x, t) dt = 0, \quad x \in (0, L) \quad (19)$$

$$\frac{dk}{dx} = 0, \quad \text{at } x = 0 \quad \text{and} \quad x = L \quad (20)$$

where g^k = Fréchet derivative of the Lagrangian with respect to k .

Next, we seek to similarly enforce the vanishing of the first variation of \mathcal{L} with respect to k_b ; this results in the following:

$$\delta_{k_b} \mathcal{L} = 0 \Rightarrow \delta k_b \int_0^T \lambda_L u|_{x=L} dt = 0 \Rightarrow \delta k_b g^{k_b} = 0 \quad (21)$$

where Eq. (17) was used, and g^{k_b} = Fréchet derivative of the Lagrangian with respect to k_b defined

$$g^{k_b} = - \int_0^T \lambda(L, t) u(L, t) dt \quad (22)$$

Eqs. (19) and (22) will vanish only when the soil properties $k(x)$ and k_b coincide with the true or target properties. In deriving Eq. (22), we used the TN scheme; if, instead, the TV scheme were used, then Eq. (22) is replaced by

$$g^k(x) = -R \epsilon \frac{d^2 k}{dx^2} \left[\left(\frac{dk}{dx} \right)^2 + \epsilon \right]^{-\frac{3}{2}} - \int_0^T \lambda u dt = 0, \quad x \in (0, L) \quad (23)$$

Implementation

Given a known pile head load $P(t)$ and displacement measurements $u_m(0, t)$, it is possible, albeit costly, to solve simultaneously the forward problem [Eqs. (1)–(3)], the adjoint problem [Eqs. (14)–(16)], and the control problems [Eqs. (19)–(22)], and obtain the soil properties $k(x)$ and k_b that would satisfy the stationarity of the Lagrangian. Here, we opt for a reduced-space method, whereby the soil properties $k(x)$ and k_b are calculated iteratively. Specifically, at each inversion iteration, the forward problem [Eqs. (1)–(3)] is solved first, using trial properties $k(x)$ and k_b . The resulting displacements $u(0, t)$ at the pile head are then used to construct the misfit $u(0, t) - u_m(0, t)$, which, as previously shown, drives the adjoint problem. The adjoint problem [Eqs. (14)–(16)] is solved next, resulting in the adjoint solution $\lambda(x, t)$. To numerically solve the forward and adjoint problems, we use finite elements to discretize in space and a Newmark scheme to integrate in time the resulting semidiscrete equations of motion.

Lastly, using the forward and adjoint solutions $u(x, t)$ and $\lambda(x, t)$, respectively, the soil properties $k(x)$ and k_b are updated using a conjugate gradient method with inexact line search that makes use of the reduced gradients g^k and g^{k_b} defined in Eqs. (19) and (22), respectively. The details of the numerical scheme are provided next.

Forward and Adjoint Discrete Problems

We appeal to a standard Galerkin procedure in order to solve numerically using finite elements the forward and adjoint problems. First, the weak form of Eq. (1) becomes

$$\int_0^L \rho A v \frac{\partial^2 u}{\partial t^2} dx + \int_0^L EA \frac{\partial v}{\partial x} \frac{\partial u}{\partial x} dx + \int_0^L k v u dx + k_b v(L) u(L, t) = v(0) P(t) \quad (24)$$

where $v(x) \in H^1(\Omega)$, where $\Omega = \{x: 0 < x < L\}$, is an admissible test function, and the boundary conditions in Eq. (2) were taken into account.

Next, we introduce standard Lagrange-family approximations $\phi(x)$ for the trial function $u(x, t)$ and test function $v(x)$; their introduction yields the classic semidiscrete form for the forward problem

$$\mathbf{M}^{\text{for}} \ddot{\mathbf{U}}(t) + \mathbf{K}^{\text{for}} \mathbf{U}(t) = \mathbf{F}^{\text{for}}(t) \quad (25)$$

where $\mathbf{U}(t)$ is the vector of nodal displacements $u(x, t)$; and the mass matrix \mathbf{M}^{for} , stiffness matrix \mathbf{K}^{for} , and force vector $\mathbf{F}(t)$ are defined, respectively, as follows:

$$\begin{aligned} \mathbf{M}^{\text{for}} &= \int_0^L \rho A \phi(x) \phi^T(x) dx \\ \mathbf{K}^{\text{for}} &= \int_0^L \left[EA \frac{\partial \phi(x)}{\partial x} \frac{\partial \phi^T(x)}{\partial x} + k \phi(x) \phi^T(x) \right] dx + k_b \phi(L) \phi^T(L) \\ \mathbf{F}^{\text{for}}(t) &= \phi(0) P(t) \end{aligned} \quad (26)$$

Following similar steps for the adjoint problem yields the following weak form of Eq. (14):

$$\int_0^L \rho A w \frac{\partial^2 \lambda}{\partial t^2} dx + \int_0^L EA \frac{\partial w}{\partial x} \frac{\partial \lambda}{\partial x} dx + \int_0^L k w \lambda dx + k_b w(L) \lambda(L, t) = w(0) [u(0, t) - u_m(0, t)] \quad (27)$$

where $w(x)$ = admissible test function. Introduction of approximations for $\lambda(x, t)$ and $w(x)$ would lead to the following semidiscrete form for the adjoint problem:

$$\mathbf{M}^{\text{adj}} \ddot{\mathbf{\Lambda}}(t) + \mathbf{K}^{\text{adj}} \mathbf{\Lambda}(t) = \mathbf{F}^{\text{adj}}(t) \quad (28)$$

where $\mathbf{\Lambda}(t)$ is the vector of nodal values of the adjoint variable $\lambda(x, t)$, and

$$\mathbf{M}^{\text{adj}} = \mathbf{M}^{\text{for}}, \quad \mathbf{K}^{\text{adj}} = \mathbf{K}^{\text{for}}, \quad \mathbf{F}^{\text{adj}}(t) = \phi(0) [u(0, t) - u_m(0, t)] \quad (29)$$

Although the forward semidiscrete form [Eq. (25)] is subject to initial conditions [Eq. (3)], the adjoint semidiscrete form [Eq. (28)] is subject to final conditions [Eq. (16)]. Clearly, the equality of the system matrices between the forward and the adjoint problems shown in Eq. (29) entails computational cost advantages, irrespective of the time integration scheme of choice.

Soil Property Updates

The continuous Winkler parameter $k(x)$, representing the varying in-depth soil stiffness, is discretized using N_s linear elements, resulting in $N_s + 1$ unknown nodal properties; thus

$$k(x) \approx \sum_{i=1}^{N_s+1} \psi_i(x) k_i = \boldsymbol{\psi}^T(x) \mathbf{k} \quad (30)$$

where $\psi_i(x)$ = basis functions; and \mathbf{k} is the vector of nodal soil property values. During each i th inversion iteration, the vector \mathbf{k} of the nodal values of $k(x)$ is updated according to

$$\mathbf{k}_{i+1} = \mathbf{k}_i + \alpha_i^k \mathbf{d}_i^k \quad (31)$$

where \mathbf{d}_i^k is the search direction vector at \mathbf{k}_i ; and α_i^k = step length in the \mathbf{d}_i^k direction. Similarly, the soil stiffness at the pile bottom k_b is updated using

$$(k_b)_{i+1} = (k_b)_i + \alpha_i^{k_b} \mathbf{d}_i^{k_b} \quad (32)$$

where $\alpha_i^{k_b}$ = step length in the direction of $\mathbf{d}_i^{k_b}$. At each iteration, the search directions are defined as the negative of the property gradients, i.e., as follows:

$$\mathbf{d}_i^k = -\mathbf{g}_i^k \quad \text{and} \quad \mathbf{d}_i^{k_b} = -\mathbf{g}_i^{k_b} \quad (33)$$

To complete the update process, it remains to define the gradients \mathbf{g}^k and \mathbf{g}^{k_b} at each inversion iteration. To this end, \mathbf{g}^k is the discrete version of the Fréchet derivative defined in Eq. (19), which is computed by collocating Eq. (19) at the $N_s + 1$ nodal points where the properties are evaluated; \mathbf{g}^{k_b} was defined in Eq. (22). At each inversion iteration, the misfit functional \mathcal{F}_m is evaluated using the updated material properties and compared against a preset tolerance. If it exceeds the tolerance threshold, then the inversion proceeds to the next iteration. We used an inexact line search with a sufficient decrease condition in the misfit functional, as measured by the following inequality (Armijo condition):

$$\begin{aligned} &\mathcal{F}_m(\mathbf{k}_{i+1}, (k_b)_{i+1}) - \mathcal{F}_m(\mathbf{k}_i, (k_b)_i) \\ &\leq \min\{\mu^k \alpha_i^k \mathbf{g}_i^k \cdot \mathbf{d}_i^k, \mu^{k_b} \alpha_i^{k_b} \mathbf{g}_i^{k_b} \cdot \mathbf{d}_i^{k_b}\} \end{aligned} \quad (34)$$

where μ^k and μ^{k_b} are typically chosen to be small values, e.g., $\mu^k = \mu^{k_b} = 10^{-10}$. If the inequality Eq. (34) is not satisfied, a backtracking procedure is performed by multiplying the step lengths (α_i^k and/or $\alpha_i^{k_b}$) by a contraction factor $\rho \in (0, 1)$ (e.g., $\rho = 0.5$) until the sufficient decrease condition is satisfied. The step lengths for $k(x)$ and k_b are determined independently because each has its own search direction. The entire inversion process discussed thus far is summarized as follows.

Algorithm 1. Inversion process for reconstructing soil stiffnesses $k(x)$ and k_b

- 1: Choose ρ , μ^k , and μ^{k_b} (e.g., $\rho = 0.5$, $\mu^k = \mu^{k_b} = 10^{-10}$)
- 2: Choose initial step lengths $\bar{\alpha}^k$, $\bar{\alpha}^{k_b}$, and regularization factor \bar{R}
- 3: Set convergence tolerance tol (e.g., $tol = 10^{-12}$)
- 4: Set the initial guess for \mathbf{k}_0 and k_{b0}
- 5: $i \leftarrow 0$
- 6: Set $\alpha_i^k = \bar{\alpha}^k$, $\alpha_i^{k_b} = \bar{\alpha}^{k_b}$, and $R_i = \bar{R}$
- 7: Set $(\mathcal{F}_m)_i = tol + 1$
- 8: **while** $((\mathcal{F}_m)_i > tol)$ **do**
- 9: Solve the state problem for $u(x, t)$ [Eqs. (1)–(3)]
- 10: Solve the adjoint problem for $\lambda(x, t)$ [Eqs. (14)–(16)]
- 11: Update the regularization factor R_i
- 12: Compute \mathbf{g}_i^k [Eq. (19) for TN, Eq. (23) for TV]
- 13: Compute $\mathbf{g}_i^{k_b}$ [Eq. (22)]
- 14: Compute the search directions \mathbf{d}_i^k and $\mathbf{d}_i^{k_b}$
- 15: **while** $[(\mathcal{F}_m)_{i+1} - (\mathcal{F}_m)_i > \min\{\mu^k \alpha_i^k \mathbf{g}_i^k \cdot \mathbf{d}_i^k, \mu^{k_b} \alpha_i^{k_b} \mathbf{g}_i^{k_b} \cdot \mathbf{d}_i^{k_b}\}]$ **do**
- 16: $\alpha_i^k \leftarrow \rho \alpha_i^k$ if $[(\mathcal{F}_m)_{i+1} - (\mathcal{F}_m)_i > \mu^k \alpha_i^k \mathbf{g}_i^k \cdot \mathbf{d}_i^k]$
- 17: $\alpha_i^{k_b} \leftarrow \rho \alpha_i^{k_b}$ if $[(\mathcal{F}_m)_{i+1} - (\mathcal{F}_m)_i > \mu^{k_b} \alpha_i^{k_b} \mathbf{g}_i^{k_b} \cdot \mathbf{d}_i^{k_b}]$
- 18: **end while**
- 19: Update material properties \mathbf{k}_i and $(k_b)_i$ [Eqs. (31) and (32)]
- 20: $i \leftarrow i + 1$
- 21: **end while**

Inversion Acceleration Schemes

We are concerned with accelerating the convergence of the inversion process, and to this end, we deploy schemes we have previously used in similar problems: specifically, we consider a regularization continuation scheme and a source frequency continuation scheme; Kang and Kallivokas (2011) have given implementational details. The aim of the regularization factor continuation scheme is to maintain a balance between the misfit functional and the regularization term in the Lagrangian: if the regularization factor becomes too small, especially during early inversion iterations, the recovered soil profiles will exhibit nonphysical fluctuations, whereas if it is too large, the profile may become overly smoothed, the misfit may not be reduced, and, consequently, the inversion process may fail to converge.

With the frequency continuation scheme, we aim at gradually refining the soil property profile by subjecting the pile to loads of incrementally higher frequency content. We first probe using lower-frequency content (still in the pass-band), and use the converged profile as initial guess for a next step, where the probing is done

Table 1. Material properties of the three-layer target soil profile used in Examples 1b, 2b, 3, and 4

Layer	Range (m)	G_s (MPa)	k (MN/m ²)	Soil type
1	$0 \leq x < 15$	40	120	Hard clay
2	$15 \leq x < 30$	60	180	Sandy clay
3	$30 \leq x < 45$	80	240	Sandy clay

using higher-frequency content. In this manner, we not only progress through the inversion with physically meaningful profiles, but also alleviate solution multiplicity.

In addition, for the first time, we experimented with alternating regularization schemes: specifically, we drive the early inversion iterations with the Tikhonov scheme to filter out spurious solutions, but switch to the total variation scheme in order to sharpen soil profiles during later inversion stages. As the numerical examples attest, alternating regularization schemes proved to be quite useful.

Numerical Examples

We discuss next results from four numerical experiments conducted using the procedure outlined in the preceding sections. Throughout, we used synthetic IR data to drive the soil characterization; in all cases, synthetic data were generated using meshes that were different from the ones used for inversion to avoid committing so-called inverse crimes. For the first two examples, we used a pile embedded in clayey soil of unknown stiffness distribution, but of known end conditions: in the first example, the pile was assumed to rest on bedrock ($k_b = \infty$), whereas in the second example, the pile was elastically supported with known k_b . The third example pertains to the most general case, where both the surrounding soil stiffness $k(x)$ and the underlain soil layer's stiffness k_b were assumed unknown, and are, therefore, inverted for simultaneously. For the last example, we report on the effect that measurement noise has on the inversion. In all cases, we use both the regularization factor and source frequency continuation schemes.

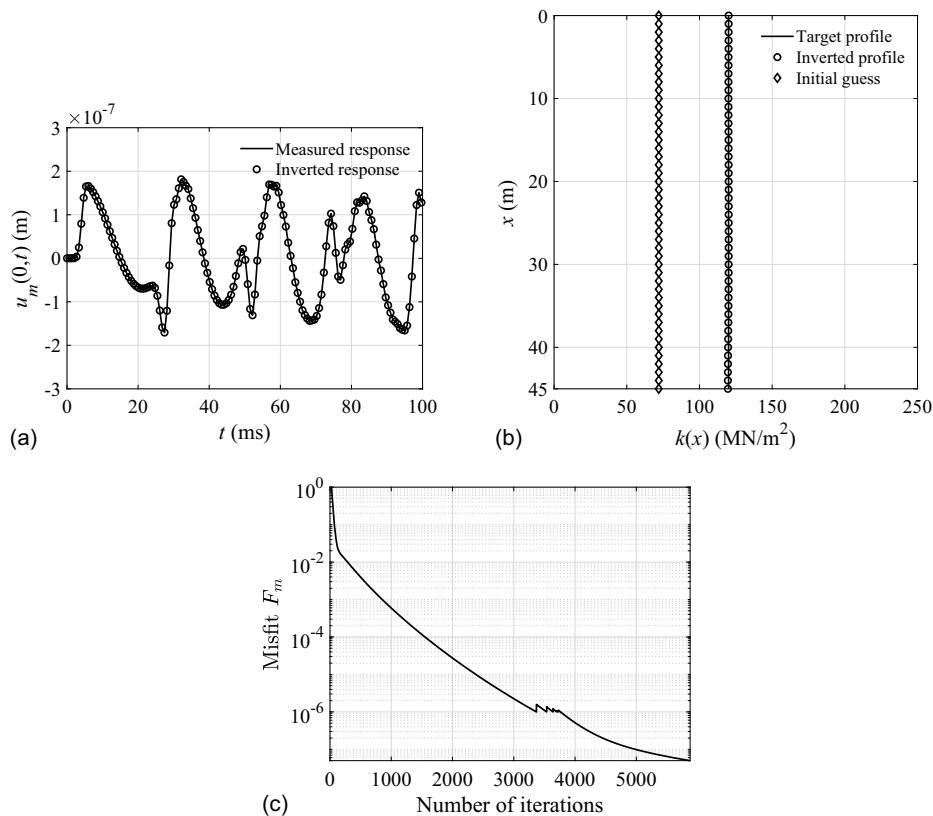


Fig. 5. Example 1a of a homogeneous soil target profile, IR data, resulting soil characterization, and inversion performance characteristics: (a) measured versus computed pile head displacements $u_m(0, t)$ for a pile embedded in homogeneous soil with $k(x) = 120$ MN/m^2 and $k_b = \infty$; (b) homogeneous soil profiles for target (solid line), inverted (circles), and initial guess (diamonds); and (c) misfit evolution.

Example 1: Pile Embedded in Clayey Soil with Fixed Bottom

We consider first the pile depicted in Fig. 1(a) for which $\rho = 2,400 \text{ kg/m}^3$, $E = 40 \text{ GPa}$, $A = 1 \text{ m}^2$, and $L = 45 \text{ m}$. The pile was assumed fixed at its end. When using a Winkler model for representing soil stiffness, there are several possibilities for assigning realistic values to the soil stiffness parameters (Anoyatis and Lemnitzer 2017); among those, we adopted a model proposed by Dobry and O'Rourke (1983) that sets the soil stiffness equal to three times the soil's shear modulus G_s . For the first example, we considered two target soil profiles, one homogeneous with constant soil stiffness $k(x) = 120 \text{ MN/m}^2$, and a layered profile, comprising three layers of equal thickness with increasing stiffness, as detailed in Table 1.

The pile head was excited with a Gaussian pulse of amplitude $p_o = 1,000 \text{ N}$. To generate the synthetic data, we used pulses with different frequency bandwidth f_b (a mathematical description of the Gaussian pulse and the definition of f_b are provided in the Appendix). To discretize the pile, we used quadratic elements with 0.225 m element length, resulting in 200 elements and 401 displacement unknowns for each forward and adjoint problem solutions. To represent the distributed soil stiffness we used 200 linear elements, resulting in 201 nodal values for $k(x)$.

Characterization of a Homogeneous Soil Profile

Fig. 5(a) shows the synthetically generated measured displacement history $u_m(0, t)$ recorded at the pile head due a Gaussian pulse with $f_b = 200 \text{ Hz}$ and the computed response corresponding to the inverted profile; as it can be seen, the agreement is excellent. Fig. 5(b) depicts the initial guess (set at $k(x) = 72 \text{ MN/m}^2$), the

target, and the inverted profiles. As can be seen, the inverted profile—reconstructed using 201 inverted-for nodal soil stiffnesses—matched the target quite accurately. To arrive at the inverted profile, we used the regularization factor continuation scheme, as well as the source frequency continuation with six distinct Gaussian pulse loads with $f_b = 200, 300, 400, 500, 600,$ and 700 Hz . Fig. 5(c) shows the evolution of the misfit during the inversion process, which exhibits a drop of about seven orders of magnitude.

Characterization of a Three-Layer Soil Profile

The inversion algorithm was also exercised to characterize the three-layer soil profile described by the properties in Table 1. Fig. 6(a) shows that the collected IR data at the pile head due to a Gaussian pulse with $f_b = 200 \text{ Hz}$ were matched closely by the computed response based on the inverted profile. Fig. 6(b) shows the reconstructed $k(x)$ profile for the layered soil medium. As can be seen, the soil profile obtained by the inversion matched exceedingly well the true profile: this includes not only the soil stiffness values, but also the layer thicknesses and layer interface locations. The inversion process was initiated with a homogeneous guess of $k(x) = 144 \text{ MN/m}^2$, and both the regularization factor continuation and the source continuation schemes were used—the latter with six Gaussian pulses with f_b ranging from 200 to 700 Hz in steps of 100 Hz. In addition, owing to the alternating use of the TN and TV regularization schemes described previously, the sharp layer interfaces have been remarkably well reconstructed. Similarly to Example 1a, Fig. 6(c) depicts the evolution of the misfit: the occasional sharp rises in the misfit correspond to switching of the source frequency content f_b , and are followed by sharp decreases, as expected.

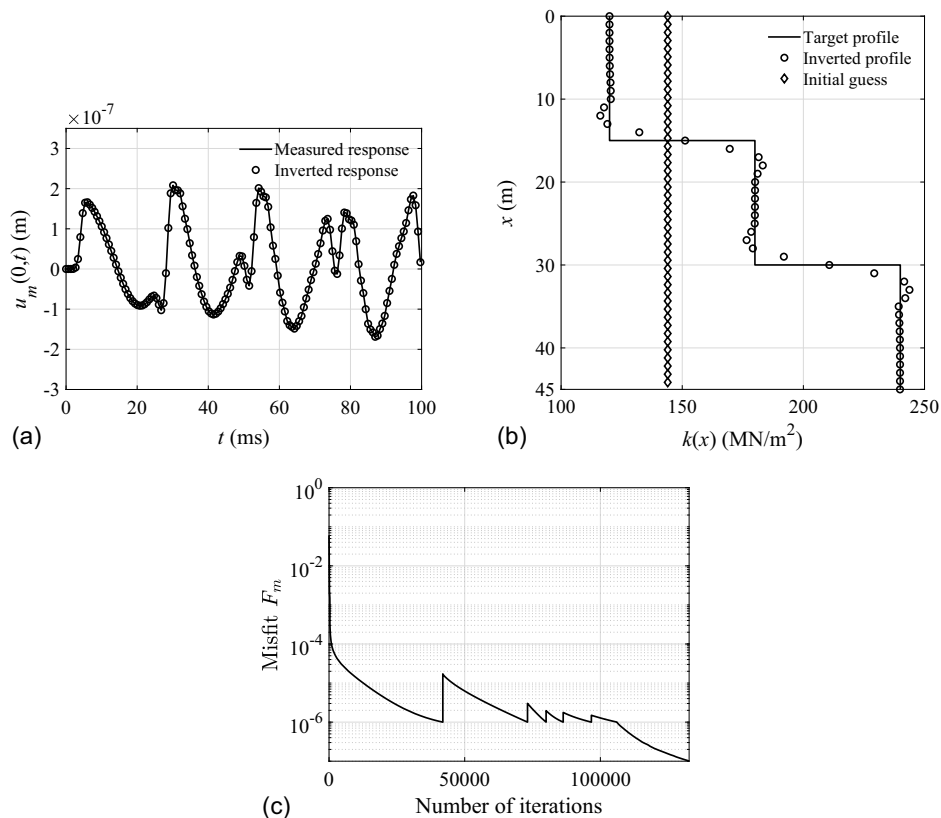


Fig. 6. Example 1b of a three-layer soil target profile, IR data, resulting soil characterization, and inversion performance characteristics: (a) measured versus computed pile head displacements $u_m(0, t)$ for a pile embedded in a three-layer soil ($k_b = \infty$); (b) three-layer soil profiles for target (solid line), inverted (circles), and initial guess (diamonds); and (c) misfit evolution.

Table 2. Material properties of the four-layer soil profile with a stiff-over-soft layer used in Example 1c

Layer	Range (m)	G_s (MPa)	k (MN/m ²)	Soil type
1	$0 \leq x < 10$	40	120	Hard clay
2	$10 \leq x < 20$	60	180	Sandy clay
3	$20 \leq x < 30$	40	120	Hard clay
4	$30 \leq x < 45$	80	240	Sandy clay

Characterization of a Four-Layer Soil Profile with a Stiff-over-Soft Layer

One of the most challenging characterization problems arises when a soft layer lies under a stiffer soil layer. Such soil layering tends to mask the presence of the soft layer, and inversion algorithms, especially when overregularized, tend to result in profiles whose stiffness increases monotonically with depth. To explore the capability

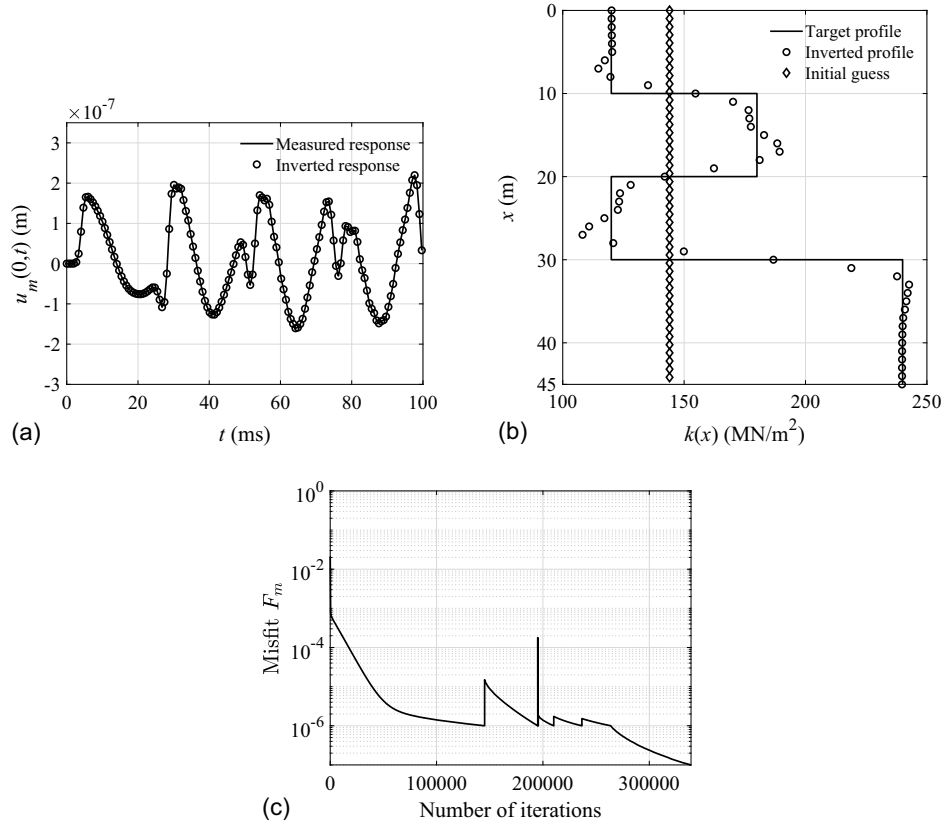


Fig. 7. Example 1c of a four-layer soil target profile with a stiff-over-soft layer, IR data, resulting soil characterization, and inversion performance characteristics: (a) measured versus computed pile head displacements $u_m(0, t)$ for a pile embedded in a four-layer soil profile with a stiff-over-soft layer ($k_b = \infty$); (b) four-layer soil profiles for target (solid line), inverted (circles), and initial guess (diamonds); and (c) misfit evolution.

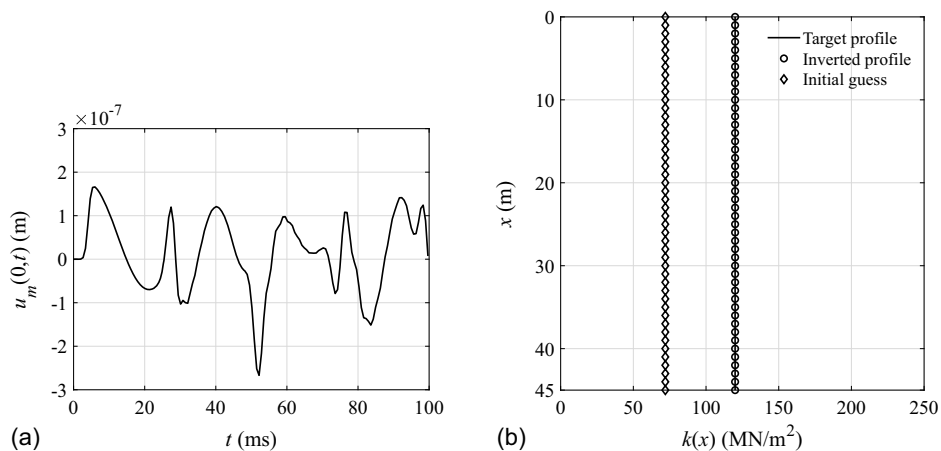


Fig. 8. Example 2a of a homogeneous soil target profile, IR data, and resulting soil characterization: (a) recorded pile head displacements $u_m(0, t)$ for a pile embedded in homogeneous soil with $k(x) = 120$ MN/m² and $k_b = 300.8$ MN/m; and (b) homogeneous soil profiles for target (solid line), inverted (circles), and initial guess (diamonds).

of our inversion scheme to capture the stiff-over-soft layering, we used the four-layer profile whose properties are described in Table 2. The soil layering included a soft layer ($20 \text{ m} \leq x < 30 \text{ m}$) sandwiched between two stiffer layers, and the bottom layer rested again on rock ($k_b = \infty$). We initiated the inversion with a homogeneous guess of $k(x) = 144 \text{ MN/m}^2$, and as before, both the regularization factor continuation and the source continuation schemes were used.

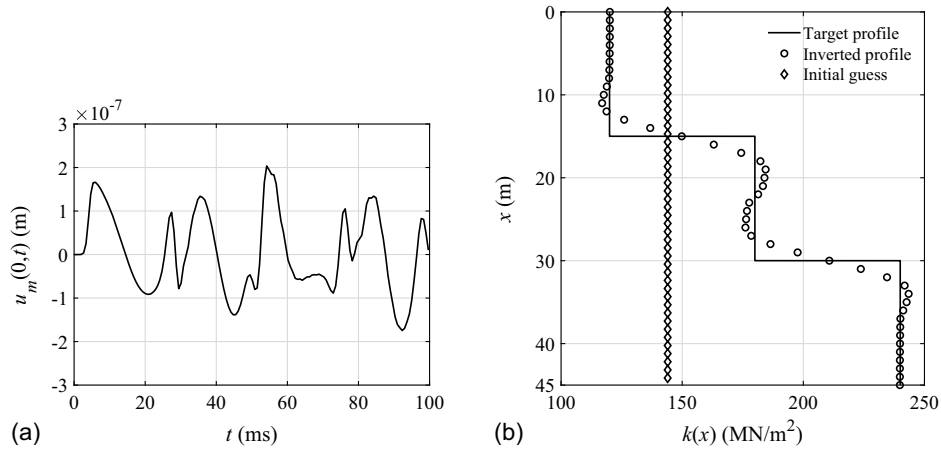


Fig. 9. Three-layer soil profiles of Example 2b for target (solid line), inverted (circles), and initial guess (diamonds): (a) recorded pile head displacements $u_m(0, t)$ for a pile embedded in a three-layer soil ($k_b = 300.8 \text{ MN/m}$); and (b) three-layer soil profile for target (solid line), inverted (circles), and initial guess (diamonds).

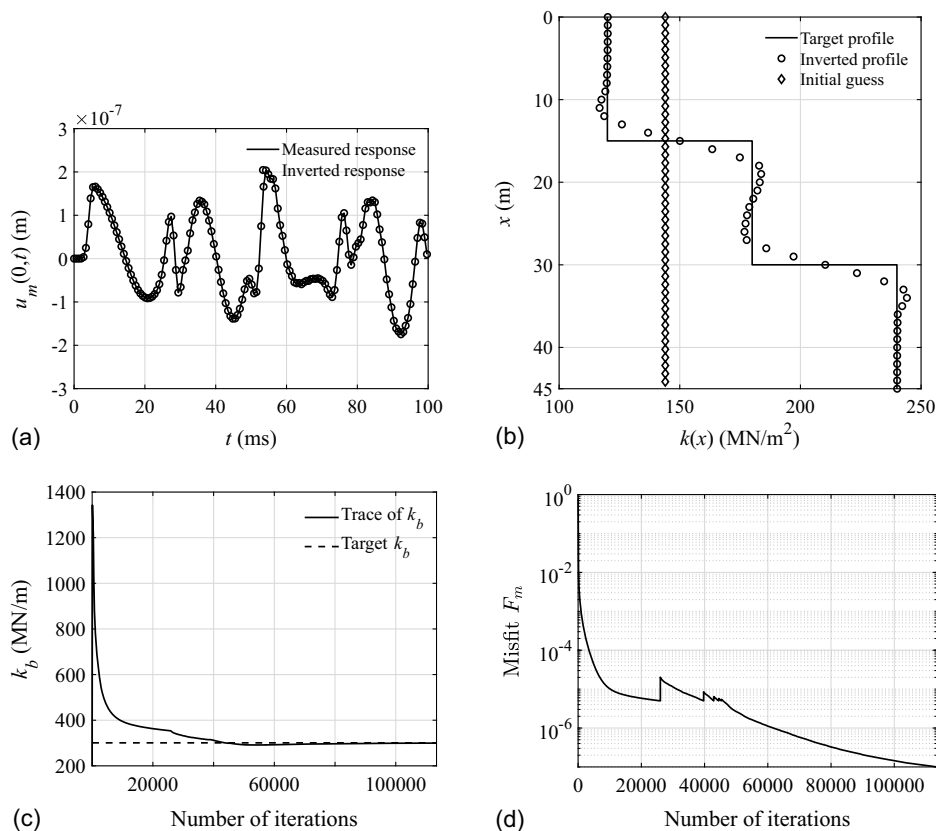


Fig. 10. Simultaneous inversion for the distributed soil stiffness $k(x)$ and the bottom soil stiffness k_b of Example 3: (a) measured versus computed pile head response; (b) three-layer soil profile of Example 3 for target (solid line), inverted (circles), and initial guess (diamonds); (c) convergence of k_b ; and (d) misfit evolution.

Example 2: Elastically Supported Pile Embedded in Clayey Soil

Next, we allowed the pile of the previous example to be elastically supported on a soil layer whose stiffness was modeled with the k_b spring, as shown in Fig. 1(b). The soil stiffness k_b can be expressed as follows (Warrington 1997; Holeyman 1988):

$$k_b = \frac{4G_s r_t}{1 - \nu_s} \quad (35)$$

where G_s and ν_s = underlying soil's shear modulus and Poisson ratio, respectively; and r_t = pile's radius at the toe. Using customary values and Eq. (35), we set k_b to 300.8 MN/m, and sought again to characterize both a homogeneous soil profile (Example 2a), and a three-layer profile (Example 2b), using the same target data as in Example 1.

Figs. 8(a) and 9(a) depict the recorded pile head IR data for the two soil profile cases, and Figs. 8(b) and 9(b) show the initial guess, the target, and the reconstructed soil profiles. As the results attest, the inversion algorithm successfully characterized the soil in the pile's vicinity with accuracy similar to the one exhibited in Example 1 for both the homogeneous and layered soils.

Example 3: Simultaneous Inversion for $k(x)$ and k_b

We attempt next to characterize simultaneously the distributed soil stiffness $k(x)$ and the underlain soil's stiffness k_b using the IR data at the pile head. The target $k(x)$ is the three-layer profile described in Table 1, and the target value of k_b was 300.8 MN/m. The measured pile head displacement time history was the same as for the

three-layer inversion of Example 2b [Fig. 9(a)]. We used a constant initial guess $k(x) = 144$ MN/m² and set the initial guess for k_b to 150.4 MN/m. Fig. 10(b) shows the reconstructed $k(x)$ profile, and Fig. 10(c) depicts the evolution of the k_b values during the inversion iterations.

As can be seen, the simultaneous inversion recovered both the three-layer soil profile and the underlain soil's stiffness reasonably well. During the early iterations, k_b increased rapidly, and then decreased gradually to the target value. The source frequency and regularization factor continuation schemes played again a critical role in the simultaneous inversion: we used consecutively the same six Gaussian pulses as in previous examples, with f_b ranging between 200 and 700 Hz, in steps of 100 Hz. The change of source frequency can be identified in the variation of the misfit shown in Fig. 10(d); it corresponds to the spikes in the curve. The source frequency was updated to the next level every time the normalized misfit was reduced to 5×10^{-6} during the inversion. Overall, the misfit was reduced from a starting value of 6.2×10^{-1} to approximately 5×10^{-7} after 130,000 iterations. To improve on the sharpness of the layer interfaces, we used the TN regularization scheme with the smallest f_b and switched to the TV scheme when processing all subsequent loads. The calculated pile head displacement obtained using the reconstructed $k(x)$ and k_b agreed well with the recorded data, as can be seen in Fig. 10(a).

Example 4: Inversion Using Noisy IR Data

Lastly, we return to the three-layer profile of Example 2b with the elastically supported pile and assess the effect of measurement

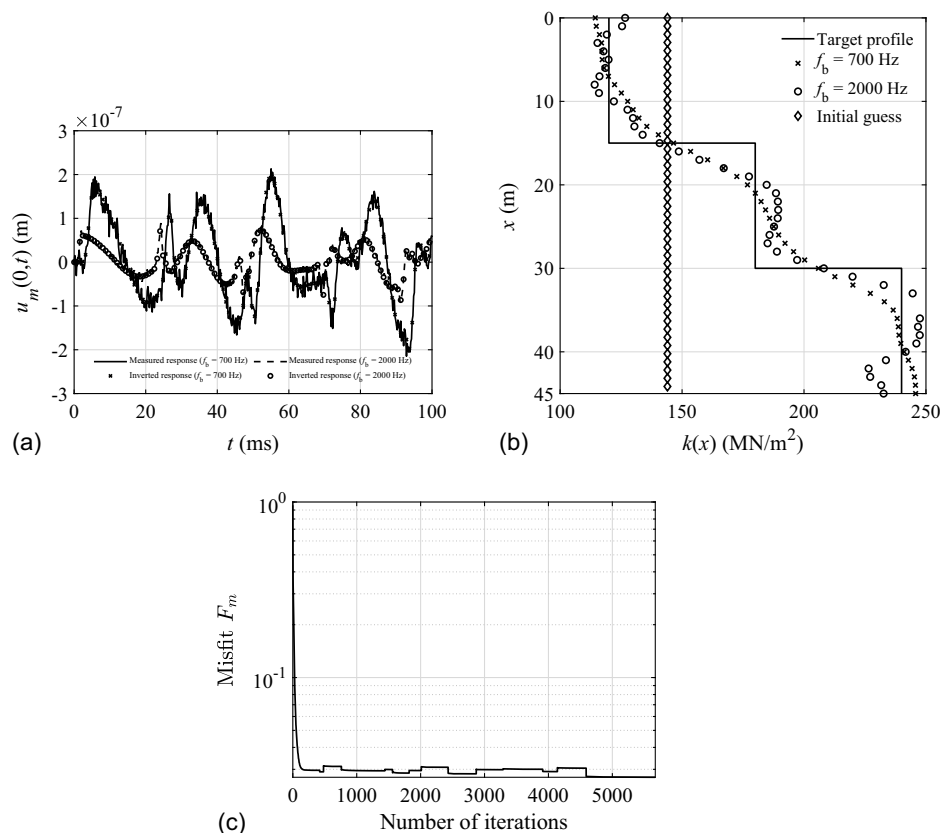


Fig. 11. Example 4: three-layer soil target profile where the pile is elastically supported and soil profiles reconstructed using noisy data: (a) measured pile head displacements $u_m(0, t)$ with 5% Gaussian noise for the three-layer target $k(x)$ profile of Example 2b versus computed displacements; (b) three-layer soil profiles for target (solid line), inverted (circles), and initial guess (diamonds); and (c) misfit evolution.

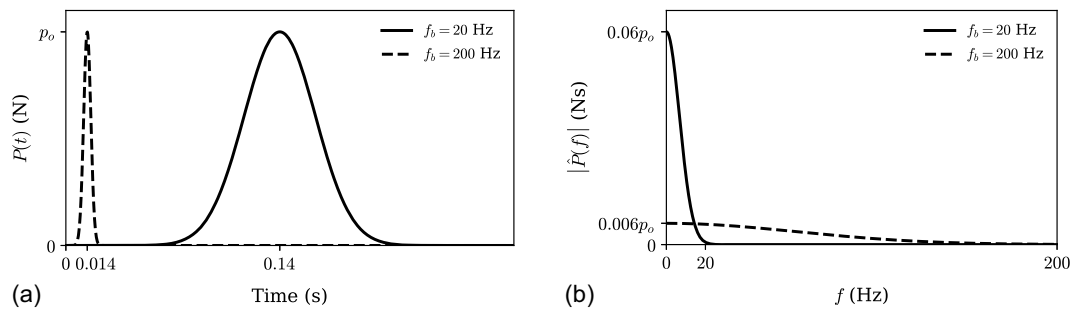


Fig. 12. Gaussian pulses with two bandwidth spectra of f_b 20 and 200 Hz (or, equivalently, for σ of 23.87 and 2.387 ms, respectively): (a) Gaussian pulse $P(t)$; and (b) Fourier spectrum $|\hat{P}(f)|$.

noise in the ability of the inversion process to reconstruct the soil profiles. Fig. 11(a) depicts the measured displacement response $u_m(0, t)$ when 5% Gaussian noise was injected. The target $k(x)$ profile was again the same three-layer profile described in Table 1, and k_b has been set to 300.8 MN/m, and is considered a priori known. Fig. 11(b) shows the target, initial guess, and inverted $k(x)$ profiles.

As before, here too we exploited the source frequency and regularization factor continuation schemes to alleviate solution multiplicity. To address the presence of noisy data, we used 13 probing Gaussian pulses—all resulting in noisy measurements—with f_b ranging from 200 to 2,000 Hz (source frequency bandwidth was incremented in 100-Hz steps between 200 and 1,000 Hz, and in 200-Hz steps between 1,000 and 2,000 Hz). The TN regularization was used in all cases. Fig. 11(c) shows the evolution of the misfit: due to the noise, the misfit was reduced to only 2.8% of its initial value. Still, as shown in Fig. 11(a) there was good agreement between the computed pile head displacements and the noisy IR data, testifying to the fact that the inversion algorithm has reasonably well-characterized the soil even in the presence of noisy data.

Conclusions

We discussed a full-waveform inversion approach for characterizing the soil in contact with a pile when given the recorded time traces of displacements at the pile head generated by short pulse loads also applied at the pile head. To model the soil, we used the Winkler hypothesis, but other soil models can be similarly accommodated. With the aid of synthetically generated pile head data, we demonstrated the ability of the developed approach to fully characterize vertically heterogeneous soils enveloping the pile, including the soil layer on which the pile is founded. The developed approach extends the potential use of the traditional IR data, under the assumption that the pile's integrity has not been compromised. Importantly, however, the approach opens the possibility for simultaneously characterizing the soil and assessing the pile's condition under a joint inversion procedure where the pile's characteristics (material and geometric properties, EA and L) are inverted for together with the soil properties.

Appendix. Gaussian Pulse Characteristics

Let $P(t)$ be defined as the Gaussian pulse described by

$$P(t) = p_o e^{-(t-6\sigma)^2/(2\sigma^2)} \quad (36)$$

where p_o = amplitude of the pulse at peak time 3σ . The amplitude $\hat{P}(f)$ of the Fourier transform of the Gaussian pulse is

$$|\hat{P}(f)| = p_o \sqrt{2\pi\sigma^2} e^{-2\pi^2\sigma^2 f^2} \quad (37)$$

Thus, in the time domain, the sharpness of the pulse is controlled by σ [Fig. 12(a)]; in the frequency domain, it can be shown that, approximately 99.7% of the pulse's spectrum lies between a zero frequency and $3/(2\pi\sigma)$ [Fig. 12(b)]. Accordingly, we define the pulse's bandwidth of interest as follows:

$$f_b = 3/(2\pi\sigma) \quad (38)$$

Data Availability Statement

Some or all data, models, or code that support the findings of this study are available from the corresponding author upon reasonable request. This includes the input data, the inversion code, and the output data.

Acknowledgments

The work of the third author was partially supported by a National Research Foundation of Korea (NRF) Grant (NRF-2017R1C1B2004975).

References

- Anoyatis, G., and A. Lemnitzer. 2017. "Kinematic Winkler modulus for laterally-loaded piles." *Soils Found.* 57 (3): 453–471. <https://doi.org/10.1016/j.sandf.2017.05.011>.
- Baxter, S. C., M. O. Islam, and S. L. Gassman. 2004. "Impulse response evaluation of drilled shafts with pile caps: Modeling and experiment." *Can. J. Civ. Eng.* 31 (2): 169–177. <https://doi.org/10.1139/l03-086>.
- Biegler, L. T., O. Ghattas, M. Heinkenschloss, and B. van Bloemen Waanders. 2003. "Large-scale PDE-constrained optimization: An introduction." In *Large-scale PDE-constrained optimization*, 3–13. Berlin: Springer.
- Bregman, N., R. Bailey, and C. Chapman. 1989. "Crosshole seismic tomography." *Geophysics* 54 (2): 200–215. <https://doi.org/10.1190/1.1442644>.
- Chin, J., and H. Poulos. 1991. "A 'TZ' approach for cyclic axial loading analysis of single piles." *Comput. Geotech.* 12 (4): 289–320. [https://doi.org/10.1016/0266-352X\(91\)90027-D](https://doi.org/10.1016/0266-352X(91)90027-D).
- Courage, W., and M. Bielefeld. 1992. "TNOWAVE automatic signal matching." In *Application of stress-wave theory to piles*, 241–246. Oxfordshire, UK: Routledge.
- Crispin, J., C. Leahy, and G. Mylonakis. 2018. "Winkler model for axially loaded piles in inhomogeneous soil." *Geotech. Lett.* 8 (4): 290–297. <https://doi.org/10.1680/jgele.18.00062>.
- Davis, A. G. 2003. "The nondestructive impulse response test in North America: 1985–2001." *NDT & E Int.* 36 (Jun): 185–193. [https://doi.org/10.1016/S0963-8695\(02\)00065-8](https://doi.org/10.1016/S0963-8695(02)00065-8).

- De Los Reyes, J. C. 2015. *Numerical PDE-constrained optimization*. New York: Springer.
- Dobry, R., and M. O'Rourke. 1983. "Discussion on 'Seismic response of end-bearing piles' by R. Flores-Berrones and R. V. Whitman." *J. Geotech. Eng.* 109 (5): 778–781. [https://doi.org/10.1061/\(ASCE\)0733-9410\(1983\)109:5\(778\)](https://doi.org/10.1061/(ASCE)0733-9410(1983)109:5(778)).
- Ekanayake, S. D., D. Liyanapathirana, and C. J. Leo. 2013. "Influence zone around a closed-ended pile during vibratory driving." *Soil Dyn. Earthquake Eng.* 53 (Oct): 26–36. <https://doi.org/10.1016/j.soildyn.2013.06.005>.
- Fathi, A., L. F. Kallivokas, and B. Poursartip. 2015. "Full-waveform inversion in three-dimensional PML-truncated elastic media." *Comput. Methods Appl. Mech. Eng.* 296 (Nov): 39–72. <https://doi.org/10.1016/j.cma.2015.07.008>.
- Fathi, A., B. Poursartip, K. H. Stokoe, and L. F. Kallivokas. 2016. "Three-dimensional P- and S-wave velocity profiling of geotechnical sites using full-waveform inversion driven by field data." *Soil Dyn. Earthquake Eng.* 87 (Aug): 63–81. <https://doi.org/10.1016/j.soildyn.2016.04.010>.
- Finno, R. J., and S. L. Gassman. 1998. "Impulse response evaluation of drilled shafts." *J. Geotech. Environ. Eng.* 124 (10): 965–975. [https://doi.org/10.1061/\(ASCE\)1090-0241\(1998\)124:10\(965\)](https://doi.org/10.1061/(ASCE)1090-0241(1998)124:10(965)).
- Hertlein, B., and A. Davis. 2007. *Nondestructive testing of deep foundations*. Hoboken, NJ: Wiley.
- Holeyman, A. 1988. "Modeling of dynamic behavior at the pile base." In *Proc., 3rd Int. Conf. on the Application of Stress-Wave Theory to Piles*, 174–185. Vancouver, BC, Canada: Bi-Tech Publishers.
- Holeyman, A. 1992. "Keynote lecture: Technology of pile dynamic testing." In *Application of stress-wave theory to piles*, 195–215. Oxfordshire, UK: Routledge.
- Holeyman, A., and V. Whenham. 2015. "Axial non-linear dynamic soil-pile interaction." In *Structural nonlinear dynamics and diagnosis*, 305–333. New York: Springer.
- Kallivokas, L. F., A. Fathi, S. Kucukcoban, K. H. Stokoe, J. Bielak, and O. Ghattas. 2013. "Site characterization using full waveform inversion." *Soil Dyn. Earthquake Eng.* 47 (Apr): 62–82. <https://doi.org/10.1016/j.soildyn.2012.12.012>.
- Kang, J. W., and L. F. Kallivokas. 2011. "The inverse medium problem in heterogeneous PML-truncated domains using scalar probing waves." *Comput. Methods Appl. Mech. Eng.* 200 (Mar): 265–283. <https://doi.org/10.1016/j.cma.2010.08.010>.
- Kausel, E. 2010. "Early history of soil–structure interaction." *Soil Dyn. Earthquake Eng.* 30 (9): 822–832. <https://doi.org/10.1016/j.soildyn.2009.11.001>.
- Liao, S.-T., and J. M. Roësset. 1997. "Impulse response evaluation of drilled shafts." *Int. J. Numer. Anal. Methods Geomech.* 21 (4): 255–275. [https://doi.org/10.1002/\(SICI\)1096-9853\(199704\)21:4<255::AID-NAG869>3.0.CO;2-J](https://doi.org/10.1002/(SICI)1096-9853(199704)21:4<255::AID-NAG869>3.0.CO;2-J).
- Lombaert, G., G. Degrande, S. François, and D. Thompson. 2015. "Groundborne vibration due to railway traffic: A review of excitation mechanisms, prediction methods and mitigation measures." In Vol. 126 of *Proc., Noise and Vibration Mitigation for Rail Transportation Systems: Proc. of the 11th Int. Workshop on Railway Noise*, 253–287. Berlin: Springer. https://doi.org/10.1007/978-3-662-44832-8_33.
- Middendorp, P., and G. Verbeek. 2004. "Thirty years of experience with the wave equation solution based on the method of characteristics." In *7th Int. Conf. on the Application of Stress Wave Theory to Piles*. Kuala Lumpur, Malaysia: World Press.
- Nazarian, S., and M. R. Desai. 1993. "Automated surface wave method: Field testing." *J. Geotech. Eng.* 119 (7): 1094–1111. [https://doi.org/10.1061/\(ASCE\)0733-9410\(1993\)119:7\(1094\)](https://doi.org/10.1061/(ASCE)0733-9410(1993)119:7(1094)).
- Park, C. B., R. D. Miller, and J. Xia. 1999. "Multichannel analysis of surface waves." *Geophysics* 64 (Apr): 800–808. <https://doi.org/10.1190/1.1444590>.
- Phuong, N., A. Van Tol, A. Elkadi, and A. Rohe. 2016. "Numerical investigation of pile installation effects in sand using material point method." *Comput. Geotech.* 73 (Apr): 58–71. <https://doi.org/10.1016/j.compgeo.2015.11.012>.
- Radhima, J., K. Kanellopoulos, and G. Gazetas. 2021. "Static and dynamic lateral non-linear pile–soil–pile interaction." *Géotechnique* 72 (7): 642–657. <https://doi.org/10.1680/jgeot.20.P.250>.
- Rausche, F. 2004. "Non-destructive evaluation of deep foundations." In *Proc., 5th Int. Conf. on Case Histories in Geotechnical Engineering*, 1–9. Rolla, MO: Univ. of Missouri Rolla.
- Rausche, F., G. Goble, and G. Likins. 1992. "Investigation of dynamic soil resistance on piles using GRLWEAP." In *Application of stress-wave theory to piles*, 137–142. Oxfordshire, UK: Routledge.
- Rausche, F., G. G. Goble, and G. E. Likins Jr. 1985. "Dynamic determination of pile capacity." *J. Geotech. Eng.* 111 (3): 367–383. [https://doi.org/10.1061/\(ASCE\)0733-9410\(1985\)111:3\(367\)](https://doi.org/10.1061/(ASCE)0733-9410(1985)111:3(367)).
- Rausche, F., B. Robinson, and L. Liang. 2000. "Automatic signal matching with CAPWAP." In *Proc., 6th Int. Conf. on the Application of Stress-wave Theory to Piles*, edited by S. Niyama and J. Beim, 53–58. São Paulo, Brazil: A. A. Balkema, Rotterdam.
- Rix, G. J., C. Lai, and W. A. Spang Jr. 2000. "In situ measurements of damping ratio using surface waves." *J. Geotech. Geoenviron. Eng.* 126 (5): 472–480. [https://doi.org/10.1061/\(ASCE\)1090-0241\(2000\)126:5\(472\)](https://doi.org/10.1061/(ASCE)1090-0241(2000)126:5(472)).
- Schevenels, M., G. Lombaert, G. Degrande, and S. François. 2008. "A probabilistic assessment of resolution in the SASW test and its impact on the prediction of ground vibrations." *Geophys. J. Int.* 172 (1): 262–275. <https://doi.org/10.1111/j.1365-246X.2007.03626.x>.
- Seylabi, E., A. Kurtuluş, K. H. Stokoe, and E. Taciroglu. 2017. "Interaction of a pile with layered-soil under vertical excitations: Field experiments versus numerical simulations." *Bull. Earthquake Eng.* 15 (Mar): 3529–3553. <https://doi.org/10.1007/s10518-017-0099-5>.
- Shahram, F. M., and K. Fakharian. 2008. "Verification of signal matching analysis of pile driving using a finite difference based continuum numerical method." *Int. J. Civ. Eng.* 6 (3): 174–183.
- Stokoe, K., E. Arnold, R. Hoar, D. Shirley, and D. Anderson. 1978. "Development of a bottom-hole device for offshore shear wave velocity measurement." In *Proc., Offshore Technology Conf.*, 1367–1380. Richardson, TX: OnePetro.
- Stokoe, K. H., S. G. Wright, J. A. Bay, and J. M. Roësset. 1994. "Axial non-linear dynamic soil-pile interaction." In *Characterization of geotechnical sites by SASW method*, edited by R. D. Woods, 15–25. New Delhi, India: Oxford & IBH Publishing.
- Takemiya, H., and Y. Yamada. 1981. "Layered soil-pile-structure dynamic interaction." *Earthquake Eng. Struct. Dyn.* 9 (5): 437–457. <https://doi.org/10.1002/eqe.4290090504>.
- Warrington, D. 1997. "Closed form solution of the wave equation for piles." M.S. thesis, Dept. of Computational Engineering, Univ. of Tennessee at Chattanooga.
- Warrington, D. C. 2016. "Improved methods for forward and inverse solution of the wave equation for piles." Ph.D. thesis, Dept. of Computational Engineering, Univ. of Tennessee at Chattanooga.
- Yu, C.-P., S.-T. Liao, and L. F. Kallivokas. 2022. "An extension of the mobility analysis of the impulse response method for coupled pile-soil integrity testing." *J. Earthquake Eng.* 26 (7): 3703–3723. <https://doi.org/10.1080/13632469.2020.1814451>.